NJC

PAPER

View Article Online
View Journal | View Issue

Cite this: *New J. Chem.*, 2018, 42, 19090

Design, synthesis, and characterization of an Fe(II)-polymer of a redox non-innocent, heteroatomic, polydentate Schiff's base ligand: negative differential resistance and memory behaviour†

Deepa Oberoi,[a] Parveen Dagar,[b] Uday Shankar,[a] Giriraj Vyas,[b] Anil Kumar,[a] Satyajit Sahu[b] and Anasuya Bandyopadhyay *[a]

In the present work, the unique negative differential resistance (NDR) and memory effect of an organic–metallic hybrid polymer based on the self-assembly of Fe(II)-ions preceded by the synthesis of a newly designed multidentate Schiff's base ligand has been reported. The polymerization process was closely monitored in an absorbance study using a UV-vis spectrophotomer. The presence of sharp isosbestic points and saturation of absorbance at 1:1 ligand to metal concentration confirmed the stepwise growth of the polymer. A model monomer Fe-complex was also developed based on the model ligand, with the aim of understanding the properties of the polymer in a better way by comparative study but surprisingly both ligand and model ligand coordinate in a different fashion with the same Fe(II)-metal ions under similar reaction conditions, though both of them have identical binding sites. It has been found that the monomer model complex is paramagnetic while the metallopolymer is diamagnetic in nature. FESEM images of thin films of the polymer revealed the presence of homogeneously distributed interparticulate mesopores which was further confirmed by surface area analysis. A long single strand of the polymer was found on the HOPG surface by AFM study. The cyclic voltammetry study indicated that both conjugated ligand and metallopolymers are electrochemically active. The bistable memory behaviour of the device fabricated on ITO has shown a negative differential resistance effect along with good RAM and ROM behaviour, showing the potential of this novel polymer as memristor.

Received 12th August 2018,
Accepted 16th October 2018

DOI: 10.1039/c8nj04106g

rsc.li/njc

Introduction

The dream of realizing a "smart world" has been motivating researchers to develop advanced materials based devices, which have an ability to combine functionality with state-of-the-art design and can sense and behave smartly. Realization of these nano-devices will not only enhance the quality of human living standards but will also provide safety and comfort, for instance, as in the case of electrochromic materials,[1–4] memristive devices,[5–7] pH responsive materials,[8–10] piezoelectric polymers,[11,12] photochromic materials,[13,14] thermochromic materials,[15,16] self-healing materials,[17] nano-electromechanical switches,[18] *etc.* Such materials, which have been designed to mimic nature and behave anisotropically, are called "smart materials". In recent decades, smart polymeric materials have gained deep interest; especially the domain of organic–inorganic hybrid smart polymers has been the focal point of the research community. Some of the excellent properties have emerged from the synergistic effect of both organic and inorganic materials, through their fusion either at the nanoscale (composite) or at the molecular level (coordination polymer). Therefore, these hybrid materials have the advantage of both of their counterparts, *viz.* ease of processing, lightweight, flexibility, and extremely high versatility in polymer's design result from the organic component while the inorganic counterpart contributes towards superior thermal and mechanical behaviour along with optical, catalytic, electrical, and magnetic properties.[19,20] The advantage of these hybrid materials is that the metal ion is directly bonded to the ligand, which results in a more organised electron cloud distribution over the covalently bonded metallopolymer backbone as compared to doped hybrid materials.[6]

The successful performance of hybrid materials in different fields[14,21–25] led to an increased thrust to explore these materials in the field of electronics[26] in order to meet the increasing

[a] *Department of Polymer and Process Engineering, IIT Roorkee, Saharanpur-247001, India. E-mail: abptsfpt@iitr.ac.in*
[b] *Department of Physics, IIT Jodhpur, Jodhpur-342011, India*

† Electronic supplementary information (ESI) available: The experimental synthetic procedure of the model ligand and the Fe-monomer complex of the model ligand and VSM data of the model ligand are provided. The SLS, FTIR, NMR, COSY spectra, FESEM of powder sample of the ligand and AFM measurements and calculations along with CV of the ligand. See DOI: 10.1039/c8nj04106g

demand for large capacity data storage.[27] Amongst these, non-volatile memristive devices[28] have received significant attention as they offer low cost synthesis, easy processability, fast switching speed, a large On/Off ratio along with longer stability and less power consumption.[29,30] In the literature it has been reported that Bandyopadhyay *et al.* observed the memristive behaviour of a directly bonded metal–organic hybrid polymer containing a redox active azo group.[6] Later, Hu *et al.* reported the multilevel memories of a hybrid polymer of PMMA and polyoxometallate (PMMA–MAPOM) with rewritable switching properties and good retention.[27] Sometimes, these hybrid materials show a Negative Differential Resistance (NDR) effect, a unique phenomenon which shows a decrease in current with increasing voltage.[31] NDR devices have tremendous potential in terms of low power memory devices and logic gate fabrication, with the existence of the bistable states.[32] However, intriguing research is still underway to develop new strategies and molecular architectures for these advanced functional hybrid memory devices.

An alternative way to enhance the desired functional properties of smart 'tailor-made' materials is to increase the area of the interactive surface. This can be achieved by a uniform porous structure of the material which provides a large surface area to volume ratio. In this regard, mesoporous materials are becoming promising candidates for the synthesis of materials showing multifunctional properties.[33,34] They have extensive ability to interact with ions/molecules/atoms/nanoparticles not only through surface but also through bulk of the materials, which helps in better conduction and movement of ions through homogeneously distributed pores. These materials have been extensively used over the years in adsorption, separation, catalysis, sensing, energy storage, biotechnology,[35,36] *etc.* Some reports on the non-volatile memory application of mesoporous structures of organic–inorganic hybrid perovskites also exist.[37]

With these considerations, the present study focusses on the design and synthesis of a novel redox non-innocent ligand[38,39] by exploiting Schiff's bases in the organic backbone. Such types of ligand can induct reversible electrochemical activity in both metal-monomers and metallopolymers.[4,40,41] This reversible electrochemical switching acts as a key to generate properties like electrochromism, memristive property, ferroelectric property, *etc.* in hybrid materials.[42–44] However, to the best of our knowledge, a comprehensive study of Schiff's base hybrid polymers for memory applications is scarce in the literature.[27]

Herein, we describe the synthesis and characterization method of a multidentate Schiff's base ligand and its Fe(II)-polymer. The motivation behind this research is to generate novel properties from the strong metal–ligand interaction, which is present in this kind of coordination polymer because of the formation of a direct covalent bond between metal ions and ligand instead of secondary interactions like van der Waals forces present in nano-metal doped organic polymer matrices. The backbone of the Fe(II) polymer is synthesized using the metal coordinated conjugated ligand, so that if any change is induced in the oxidation state of the metal ion by external stimuli in the metallopolymer, then that message would be passed on to other metal ions present in the same polymer chain at a faster rate through the same conjugated organic backbone. Each ligand is coordinated with two different Fe(II)-centres at the same time and linear growth of the polymer is possible by self-assembly of each Fe(II)-centre with one-half of two ligands. In this report, we are introducing a unique, redox non-innocent, diamagnetic, mesoporous Fe(II)-polymer with all required characteristics for future application as a multifunctional material.

Experimental section

Materials

4,4-Dihydroxybiphenyl, hydrazine monohydrate and *N*,*N*-dimethylacetamide (*N*,*N*-DMAc), tetra-ethyl orthosilicate and 2-hydroxy-1-naphthaldehyde were purchased from TCI Chemicals (India) Pvt. Ltd and used as received. Fe(II) acetate and Pd/C were purchased from Sigma-Aldrich, India. Celite, sodium bicarbonate ($NaHCO_3$) and sodium metal were purchased from Merck Ltd, India. Nitric acid (HNO_3) was purchased from Rankem, India. All the solvents were of AR grade and purified by standard procedures wherever specified. Solvents were purchased from Merck, India. Double distilled water was used wherever required.

Instrumentation and characterization

The Fourier transform infrared spectra of the ligand and polymers were recorded on a PerkinElmer FT-IR C91158 spectrophotometer using KBr pellets, in the range of 4000–400 cm^{-1}. ^1H NMR, ^{13}C NMR and H–H COSY spectra were measured using a Bruker 400 Hz system with tetramethylsilane (TMS) as a reference. The wide angle X-ray diffraction (WXRD) patterns of the sample were collected by using a RIGAKU ULTIMA IV X ray diffractometer, in the angle range of 2θ = 5–80° at a scan rate of 4° min^{-1}, using Ni filtered CuKα as a radiation source. The absolute molecular weight of the polymer sample was recorded by Static Light Scattering (SLS) experiment in batch mode using a Brookhaven BI-200SM goniometer using filtered stock solution and solvent filtered through a 0.2 micron Nylon filter. The UV measurements were made on a UV spectrophotometer (UV-1800, Shimadzu Corp., Japan). Cyclic voltammetry (CV) measurements were performed using a cyclic voltammeter (CH1620D, CH Instruments). Atomic Force Microscope (AFM) imaging of the polymer was carried out on a freshly cleaved Highly Ordered Pyrolytic Graphene (HOPG) substrate using a NT-MDT-INTEGRA Microscope in a tapping mode at room temperature. Field Emission Scanning Electron Microscope (FESEM) images of the sample were recorded on TESCAN MIRA 3, by pouring a 10^{-5} M solution of the sample on glass slides of area 1 cm^2 mounted on stubs and sputtered with gold using a vacuum sputter. Energy Dispersive X-Ray (EDX) spectroscopy was used to determine the Fe content in the polymer sample, attached to the FESEM unit. Surface area and pore size distribution analysis of the samples were performed using a Quantachrome Autosorb IQ2 using N_2. Vibrating Sample

Magnetometer (VSM) Quantum Design PAR 155 was used to determine the magnetic moment of the samples.

Synthesis of the ligand

3,3′-Dinitrobiphenyl-4,4′-diol (1). For the synthesis of the dinitro derivative of 4,4-biphenol, a simple route has been followed with the modification of the synthetic procedure.[45] Nitric acid (70%, 2 ml) was added dropwise to a solution of 4,4′-dihydroxybiphenyl (5.4 mmol, 1.0 g) in 20 ml of glacial acetic acid, with vigorous stirring over a period of an hour at room temperature. After the complete addition, the stirring was continued at room temperature for about three hours to complete the nitration. Then 150 ml of water was added to the above solution and stirring was continued for about three hours at 50 °C. The reaction mixture was then cooled to room temperature and filtered. Precipitates were then washed with an adequate amount of water followed by ethanol and saturated aqueous solution of $NaHCO_3$. Then yellow colored precipitates were collected. Yield: 90% (1.3 g). FTIR (KBr, cm^{-1}): 3431, 3251, 1626, 1528, 1470, 1309, 1241, 1173. ^{1}H NMR (400 MHz, d_6-DMSO) δ: 11.11 (s, 2H, OH), 8.10 (d, 2H, J = 2.4 Hz), 7.83 (dd, 2H, J = 8.7 Hz), 7.15 (dd, 2H, J = 8.7 Hz). ^{13}C NMR (400 MHz d_6-DMSO) δ: 151.8, 137.9, 133.24, 129.62, 122.97, 120.15.

3,3′-Diaminobiphenyl-4,4′-diol (2). To a stirred solution of 3,3′-dinitrobiphenyl-4,4′-diol (1.38 g, 5 mmol) in ethanol, Pd/C (0.12 g, 5 mmol) was added followed by the slow addition of hydrazine monohydrate (5.5 ml).[46] After the complete addition, the mixture was heated and stirred at 85 °C. After 24 h, *N*,*N*-DMAc was added slowly to the suspension until dark grey precipitates appeared in the solution and addition of solvent was continued until all the precipitates were completely dissolved.[46] The final hot solution was filtered through celite and then it was evaporated in a rotary evaporator to reduce the volume of the solution to its half and later on added into the ice-cold water. White precipitates were washed thoroughly with distilled water and dried in an oven. Yield: 70% (75 mg). FTIR (KBr, cm^{-1}): 3378, 3290, 1592, 1509, 1441, 1280, 1221, 904, 811. ^{1}H NMR (400 MHz, d_6-DMSO) δ: 8.89 (broad (br), s, 2H, OH), 6.71 (dd, 2H, J = 2.2 Hz), 6.59 (d, 2H, J = 8.1 Hz), 6.49 (dd, 2H, J = 8.1 Hz), 6.49 (dd, 2H), 4.47 (br, s, 2H, NH_2). ^{13}C NMR (400 MHz, d_6-DMSO) δ: 143, 137, 133, 115, 112, 114.

Synthesis of ligand 3,3′-bis(((2-hydroxynaphthalen-1-yl)-methylene)amino)-[1,1′-biphenyl]-4,4′-diol (L1). The Schiff's base ligand (**L1**) has been synthesized by the reaction of 3,3′-dinitrobiphenyl-4,4′-diol (2 mmol, 0.432 g) with 2-hydroxy-1-naphthaldehyde (4 mmol, 0.744 g) in dry EtOH (20 ml) in a three neck flask equipped with a condenser, under a N_2 atmosphere. Tetraethyl orthosilicate (6 ml) was added to this solution mixture and then it was refluxed for about 6 h. After the consumption of initial reactants, the solvent was removed by using a rotary evaporator and the obtained crude mass was dried in an oven for about an hour. Then the solid mass was recrystallized from ethanol three times to get a pale-yellow product. Yield 73% (1.5 g). FTIR (KBr, cm^{-1}): 3431, 1622, 1544, 1350, 1236, 1265, 1236, 1121, 1157. ^{1}H NMR (400 MHz, d_6-DMSO) δ: 15.81 (d, J = 9.6 Hz, 1 H), 10.40 (s, 1H), 9.66 (d, J = 9.7 Hz, 1H), 8.50 (d, J = 8.3 Hz, 1H), 8.25 (d, J = 1.9 Hz, 1H), 7.79 (d, J = 9.4 Hz, 1H), 7.66 (dd, J = 7.9 Hz, 1.0 Hz, 1H), 7.49 (dd, J = 8.4 Hz, 2.1 Hz, 1H), 7.44 (t, J = 7.6 Hz, 1H), 7.25 (t, J = 7.6 Hz, 1H), 7.05 (d, J = 8.3 Hz, 1H), 6.77 (d, J = 9.3 Hz). ^{13}C NMR (400 MHz, d_6-DMSO) δ: 178, 150, 147, 138, 134, 132, 129.3, 129, 128, 126, 125.5, 125, 123, 120, 116, 115, 114, 108.

Fe(II) polymer [Fe(II)-poly]

The polymer of the above ligand was prepared by the addition of 300 mg (0.572 mmol) of Schiff's base ligand in dry ethanol, followed by the addition of 8–10 ml of NEt_3 in a nitrogen atmosphere. The mixture was stirred for about an hour. Then 100 mg (0.572 mmol) of $Fe(OAc)_2$ was added to the above mixture and was kept under reflux for about 24 h. The brown precipitates so obtained were dried and washed several times with hot ethanol yielding 0.32 g of the product (yield: 80%). FTIR (KBr, cm^{-1}): 3438, 1614, 1514, 1400, 1344, 1257, 1123, 1085, 798. ^{1}H NMR (400 MHz, d_6-DMSO) δ: 15.81 (br, 1H), 10.40 (br, 1H), 9.66 (br, 1H), 8.50 (br, 1H), 8.25 (br, 1H), 7.79 (br, 1H), 7.66 (br, 1H), 7.49 (br, 1H), 7.44 (br, 1H), 7.25 (br, 1H), 7.05 (br, 1H), 6.77 (br, 1H). Molecular weight as obtained by SLS was 68 000 g mol^{-1} (approx.) (for Berry plot *vide* Fig. S1, ESI†).

Degree of polymerization (molecular weight/repeating unit weight), $n \approx 120$ (approx.).

Device fabrication

Indium tin oxide (ITO) coated substrates were used for device fabrication. ITO was selectively etched to form a stripe by using concentrated HCl and Zn dust. After etching, the substrate was cleaned using a standard cleaning procedure, *i.e.* ultrasonication with soap solution, then rinsing with de-ionized (DI) water, followed by cleaning the substrate with acetone, DI water, and methanol using an ultrasonicator, thrice with each solvent and each time for 15 minutes. The cleaned substrates were then dried in a vacuum oven at 70 °C for 4–5 hours. These cleaned substrates were then used to deposit the organic material on them. A 25 mg ml^{-1} Fe(II)-poly in DMSO solution was prepared for the deposition of the film. The films were spin coated over the substrate at a rotational speed of 1000 rpm. The spin coated samples were kept under vacuum overnight. An 85 nm thick aluminium (Al) layer was thermally evaporated on the spin coated films. For the deposition of Al a shadow mask was used which gave us a cross-bar architecture. The effective area of the device was 0.25 cm^2. So, for the device ITO acts as the bottom contact and Al acts as the top contact. The *I–V* characterization of the sample was carried out by using a two-probe measurement technique where a Keithley 6430 Femto-ampere source meter was interfaced with a vacuum probe station. Five such devices were prepared and their electrical measurements were analysed at room temperature, under ambient conditions.

Results and discussion

The ligand (**L1**) was designed with the aim of developing a new organic molecule with three coordination sites, *viz.* N, O, O,

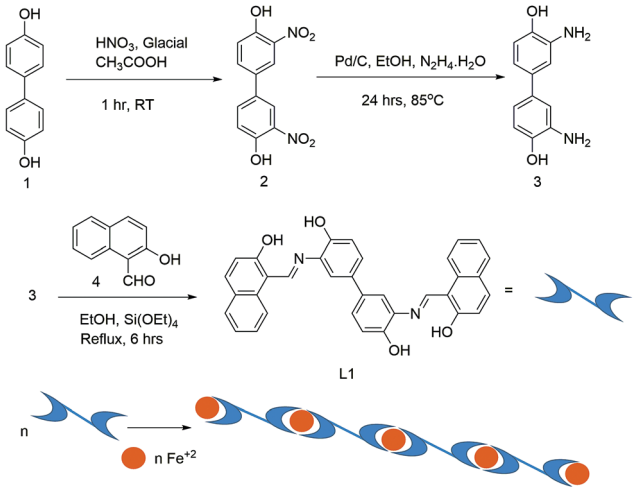

Scheme 1 Schematic representation of synthesis of the ligand and Fe(II)-poly.

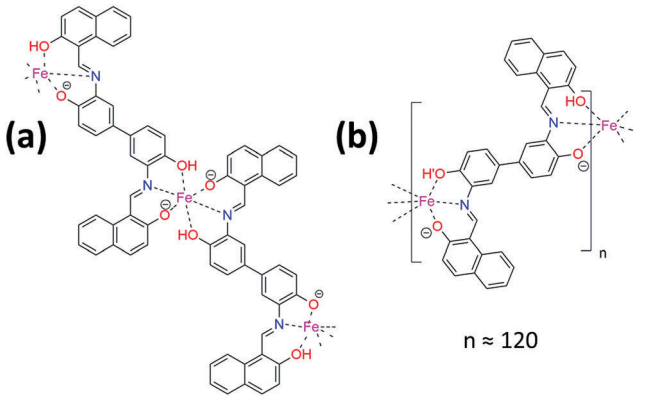

Scheme 2 (a) Schematic representation of the possible Fe(II)-poly structure, (b) representation of the monomer unit of Fe(II)-poly with n = 120 units.

in each half of the ligand and with the potential to bind with a variety of hard/soft metal ions for construction of different organic–metallic hybrid polymers. Both ligand and Fe(II)-poly were characterized by various characterization techniques (Scheme 1).

When the metal and ligand were taken in 1 : 1 proportion for polymerization reaction, the expectation was that all the –OH groups in the ligand will first get deprotonated and then they will coordinate as $-O^{-1}$ monoanionic donors, but the presence of the broad, characteristic signal of the –OH group in FTIR and hydroxyl protons in NMR experiments was opposite to our expectation and both these experiments confirmed the presence of hydroxyl protons in Fe(II)-poly. As the obtained polymer is a neutral coordination polymer and it is a diamagnetic material (NMR active), we propose the structure of the polymer as per Scheme 2, which can support both the experimental results.

Our developed organic ligand can be divided into two coordination halves and each half has three coordinating sites, N, O, O. Then, to complete the coordination number of Fe(II)-ions, two different ligands with one-half of each have to be coordinated to the same metal center, while the other half of both the ligands is coordinated to two different metal centres. This way a linear polymer chain will grow with continuous self-assembly between metal centers and organic ligand. If all four –OH groups will get deprotonated as per expectation, then the neutral complex will only be made with the Fe(IV)-metal center, which is the d^4 system. Then, the metallopolymer would become paramagnetic as Fe(IV) will make a low spin octahedral complex with the hard N,O,O donor ligand with two unpaired electron on metal center. The same complex with the Fe(II) center (d^6) metal ion will only be neutral if each ligand will coordinate as monoanionic hexacoordinated binding sites, where one hydroxyl group of the ligand will coordinate as a neutral hydroxyl group and the other one will be a hard, monoanionic $-O^{-1}$ site. The proposed structure is also diamagnetic in nature and can provide support for the presence of hydroxyl signals in FTIR and NMR studies. A detailed discussion of this study has been provided separately in the NMR studies section.

All the characterization studies have been summarized below:

FTIR studies

The overlay FTIR spectra of the ligand and polymer are provided in ESI,† Fig. S2. The FTIR spectrum of the ligand shows a broad peak at 3431 cm^{-1} owing to the presence of the –OH group, a peak at 1630 cm^{-1} due to –C=N stretching vibrations while another at 1236 cm^{-1} due to –C–N stretching vibrations. However, a slight shift has been observed in these peaks upon coordination to the metal ion.[47] The broad peak of the –OH group at 3431 cm^{-1} in the ligand is shifted to 3438 cm^{-1} in Fe(II)-poly and another peak at 1622 cm^{-1} of the ligand is shifted to 1614 cm^{-1} in Fe(II)-poly, which is an indication of stretching of the –C=N double bond on coordination of the imine moiety to the metal ion. A strong peak at 798 cm^{-1} has been observed in the fingerprint region of the polymer, arising due to the bending vibration of the Fe–OH group.[48]

NMR studies

NMR characterization of the ligand, deprotonated ligand and polymer was performed as shown in Fig. 1. Because of the presence of symmetry, all the compounds showed peaks for one-half of the ligand only. The conjugated ligand shows a doublet at 15.82δ due to the presence of the phenolic –OH (C2) group, and a second hydroxyl group –OH′ (C-13) gives a sharp singlet at 10.40δ. The difference in the nature and position of two hydroxyl groups is originated from the hydrogen bonding interaction of one (C-2) with the neighbouring imine N while the other is deprived of that interaction as two of them cannot participate in hydrogen bonding with the same imine group at the same time. Again, hydrogen bonding interaction of the –OH group attached to C2 with imine N is through six-member ring formation while the same with a second hydroxyl group makes a five membered ring. As the five-membered ring is less stable than the six membered ring, exclusively only –OH (C2) is taking part in hydrogen bonding. The effect of keto–enol tautomerism

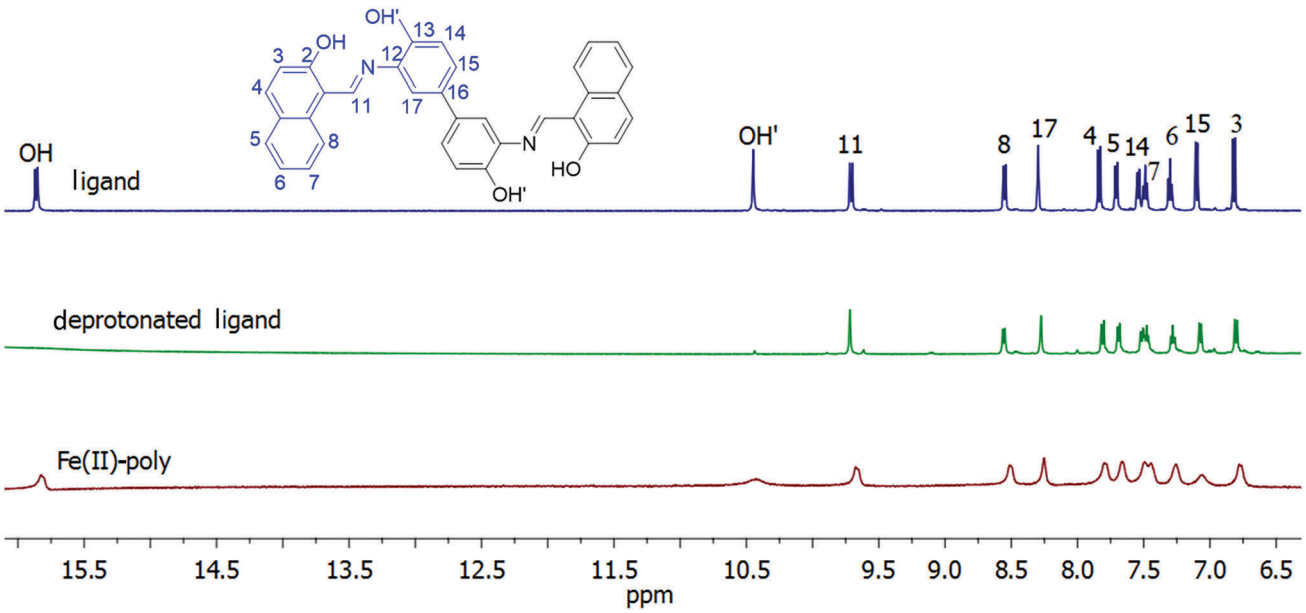

Fig. 1 Overlay ^{1}H NMR spectra of the ligand, deprotonated ligand and Fe(II)-poly in DMSO-d_6.

(*vide* Fig. S3, ESI†) is also observed in the imine proton peak.[49] As the imine proton (C11) has no neighbouring proton, only a singlet was expected in the NMR signal but it gives a doublet because of keto–enol tautomerism. To confirm hydrogen bonding interaction of the hydroxyl proton and the imine nitrogen, the ligand was completely deprotonated with triethyl amine. The NMR signal of the deprotonated ligand does not show any hydroxyl proton peak and the imine proton shows a sharp singlet as in the absence of hydroxyl proton it is not possible to start keto–enol tautomerism. All the other peaks in the deprotonated ligand are of the same type as found in the original ligand. The full designation of rest of the peaks has been done by ^{13}C NMR spectroscopy (*vide* ESI,† Fig. S3) and H–H COSY NMR spectroscopy (*vide* ESI,† Fig. S4).

In the case of Fe(II)-poly, very broad peaks are observed in the NMR spectrum which are characteristics of the polymeric sample. As the –OH (C2) proton exclusively takes part in the hydrogen bonding interaction with imine N, the acidity of this proton is more than that of the second hydroxyl proton. Therefore, when the ligand coordinates to the metal ion, first this hydroxyl group of one-half of the ligand is deprotonated and this half is donating as a tridentate, monoanionic binding site. To complete the primary and secondary valency of Fe(II), one-half of the second ligand is also deprotonated and coordinates to the same center metal ion. Now, after coordination of one-half of one ligand to the centre metal ion as a monoanionic ligand, the acidity of –OH′ (C13′) is increased more than that of –OH (C2) in the second half of the ligand. So, the other half of each coordinated ligand gets deprotonated through the –OH′ (C13′) group (Scheme 2) and the second hydroxyl group (C2′) in the other half of the ligand is coordinated as the neutral site by donating its lone pair only. For this reason, both hydroxyl proton peaks are observed in the NMR spectrum of Fe(II)-poly instead of only one. To check the reproducibility of the result different aliquots of Et_3N were added to completely deprotonate the ligand first and then polymerization reaction with $Fe(OAc)_2$ was done, but each time NMR spectra remained unaltered, which supports that the proposed structure is the best adopted coordinated form and Fe(II)-poly is only stabilized in the supramolecular structure with the conjugated backbone as the soft Fe(II) cation to minimize steric strain in the organic moiety. When the monomeric Fe complex of the model ligand was synthesized under identical conditions as for Fe(II)-poly preparation, then every time paramagnetic monomer complex was obtained. This means that the deprotonated model ligand (**L2**) has the best interaction and crystal field stabilization with hard Fe(III) cations but in the case of the polymer to minimize steric strain in the hexadentate ligand structure, the deprotonated ligand (**L1**) accepts a proton from solvent during the reaction to minimize the strain.

To further simplify the analysis of the ligand, a model ligand has been synthesized and analyzed by NMR and VSM characterization (*vide* ESI,† Scheme S1 and Fig. S5, S7). The NMR of the C-2, C-13 and C–H imine proton of the model ligand shows a similar nature to that of the ligand, with a small chemical shift. This small shift is arising as the model ligand has a structure which is half of the original ligand and thus lacks extensive conjugation which is present in the original ligand. The Fe-complex (monomer) of this model ligand has also been prepared by using identical reaction conditions (*vide* ESI,† Scheme S2 and Fig. S5). The NMR characterization of this monomeric iron complex shows sharp peaks in the range of -10δ to $+35\delta$ thereby indicating that this model monomer complex is paramagnetic in nature (*vide* ESI,† Fig. S6). These sharp ^{1}H peaks with a moderate paramagnetic shift signify the presence of low spin Fe(III).[50] So, the model ligand can stabilize the metal in +3 oxidation state while Fe(II)-poly remains in +2 oxidation with the original ligand under identical reaction conditions.

As the model ligand is only half portion of the original ligand, so one ligand can coordinates to only one metal centre in the monomer complex and this sole metal coordination makes it easier for the model ligand to lose two/one proton(s) and coordinate as tridentate, monoanionic from one side and tridentate, bisanionic from another side to the Fe(III)-center to attain more Crystal Field Stabilization Energy (CFSE). In this fashion the basicity of the ligand is increased and bonding with the metal is stronger because the metal is also present in a higher oxidation state compared to Fe(II)-poly. In the case of Fe(II)-poly, the hexacoordinated conjugated, bulkier ligand is simultaneously coordinated to two different metal centres and because of that a very close approach of the ligand to the metal is not possible as that would increase steric strain in the totally conjugated backbone of the metallopolymer. So, in the case of Fe(II)-poly, the ligand (**L1**) is coordinating in the hexadentate, bisanionic state, while the model ligand is coordinated in the tridentate, tris anionic state in the Fe-monomer metal complex.

Study of photophysical properties

After confirming the structure from IR and NMR studies, the absorption spectra of 10^{-5} M solution (DMSO/water, 1/9 v/v) of both ligand and Fe(II)-poly have been recorded at room temperature and compared with the absorption spectrum of the deprotonated ligand, by adding the required amount of triethylamine to the ligand (Fig. 2), to understand the absorption behavior of the ligand upon co-ordination with the metal ion.

The UV spectrum of the ligand shows four major bands at wavelengths 243, 316, 453 and 480 nm. The band at 243 nm arises due to the π–π* transition of naphthalene/aromatic rings. The 316 nm and 343 nm bands arise due to the π–π* transition of the –C═N group of the ligand. The bands at 453 and 480 nm arise due to the n–π* transition of the –C═N bond. In the case of the deprotonated ligand, a variation in the spectral peak is observed compared to the spectrum of the free ligand because of the lack of hydrogen bonding interactions upon deprotonation.

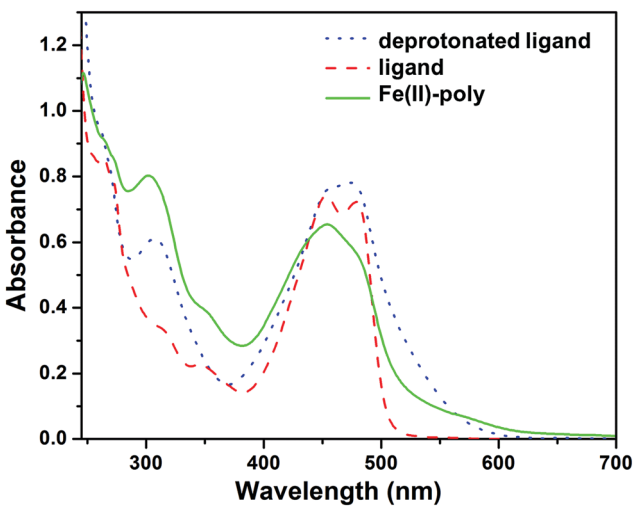

Fig. 2 Absorption spectra of 10^{-5} M solution of ligand, deprotonated ligand and Fe(II)-poly in DMSO : methanol (1 : 9).

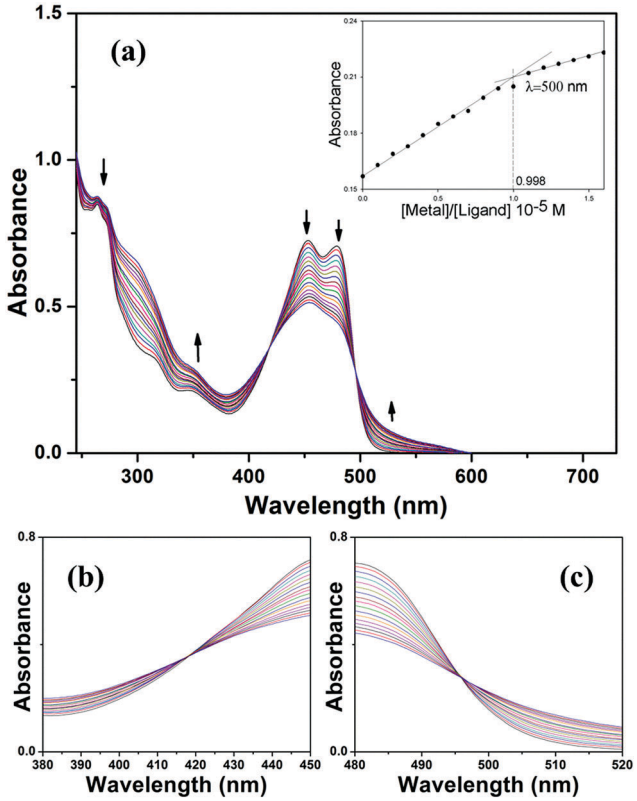

Fig. 3 (a) UV-vis titration of $Fe(OAc)_2$ with the Schiff's base ligand (10^{-5} M) in DMSO/methanol with the Job's plot in the inset, (b) and (c) sharp isosbestic points at wavelength 417 nm and 496 nm respectively.

The spectral behavior of Fe(II)-poly is a combination of both protonated and deprotonated ligand spectra with a slight shift because of co-ordination to Fe(II)-ions. The band at 483 nm disappeared in the polymer spectrum because of the involvement of non-bonding electrons with the metal ions upon coordination, and another broad low energy, low intensity transition in the NIR region has been generated at 918 nm (*vide* ESI,† Fig. S8) which is due to metal-to-ligand charge-transfer (MLCT) transition (from the d-orbital of the metal to the π* orbital of the ligand).

After the confirmation of the metal complex, the nature of complexation between the metal ion and the ligand was determined by the UV-titration method (Job's plot) (Fig. 3). To a methanolic solution of the ligand, iron(II)-acetate solution was consistently added until an equimolar stoichiometry of ligand/metal ion (1 : 1) is observed. During the titration process, two sharp isosbestic points at wavelengths 419 nm and 495 nm appeared. The observed response at 500 nm wavelength was plotted against metal to ligand proportion (Fig. 3, inset), which clearly shows saturation of absorbance intensity at ligand/metal equimolar concentration, *i.e.* 1 : 1 concentration. The band at 243 nm has been red shifted to 264 nm with the hypsochromic shift. A new red shifted band at 345 nm appeared with a slightly higher intensity during titration.

An additional increase in peak height after 500 nm wavelength in UV titration spectra was also observed due to M–L

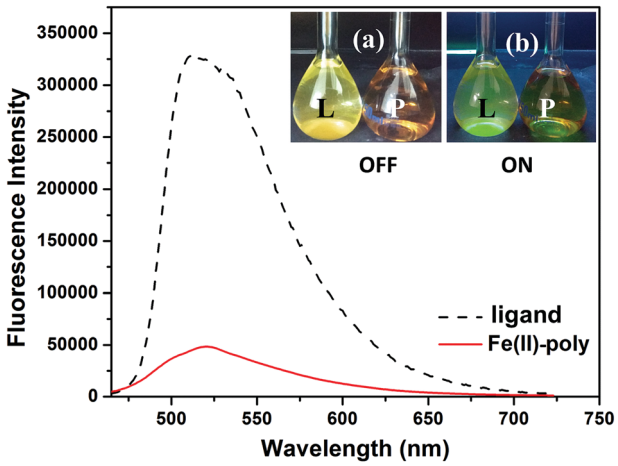

Fig. 4 Comparison of emission properties of the ligand and Fe(II)-poly excited at 465 nm, with the inset showing the color of the ligand and polymer in the UV chamber with L designating the ligand and P Fe(II)-poly.

charge transfer transition, which also justifies the formation of the complex. Shifting of the UV bands during the titration shows the formation of a complex between the Fe(II)-ions and the –OH group of the naphthalene ring and a –C═N bond.

The emission properties of the ligand and Fe(II)-poly are shown in Fig. 4. Both the ligand and polymer were excited at wavelength 465 nm and it has been found that the fluorescence shown by the ligand has been significantly quenched in Fe(II)-poly because of intermolecular interactions between the multidentate Schiff's base ligand and the Fe(II) ion,[51] thereby causing a radiation-less decay through internal conversion (IC).

XRD studies

In order to observe the crystalline behavior of both ligand and polymer, the patterns of XRD were obtained by using an X-ray diffractometer. The overlay results of the XRD pattern of both ligand and polymer are shown in Fig. 5.

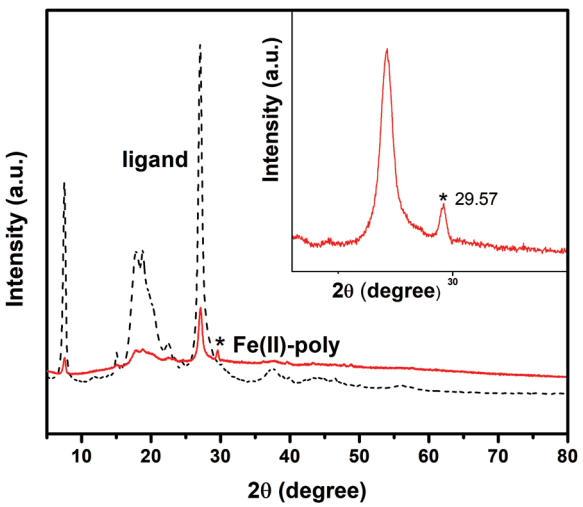

Fig. 5 XRD graph of Fe(II)-poly and the ligand; the inset shows the XRD peak due to stacking of the conjugated aromatic system.

The XRD pattern of the Fe(II)-poly shows similar peaks as that of the ligand except that there is a huge drop in intensity for the Fe(II)-poly. However, an additional peak at 29.57° is found in the metal polymer, which is due to stacking of the conjugated aromatic system in the polymer.[52,53] This also clearly points towards the existence of host–guest interactions between the Fe(II) units and the multidentate organic ligand by direct bond formation between them and the absence of formation of any aggregate because of weak secondary interactions between the metal ion and the ligand.

As the XRD pattern of Fe(II)-poly shows only broad diffraction peaks, which indicate amorphous nature of polymer and it has also been suggested that various π–π stacking structures are expected in between the hybrid polymer chains.[54] The XRD pattern of Fe(II)-poly exhibits its amorphous nature, so our various attempts to grow single crystals were in vain.

Surface morphology

The morphological study of the polymer surface was performed by various characterization techniques such as FE-SEM, AFM and BET surface area analysis. A thin film of polymer was grown on a glass substrate by pouring a well sonicated dilute (10^{-5} M) solution prepared in methanol:DMSO solvent and later dried in air for about four to five hours. The images obtained from surface studies by different techniques are shown in Fig. 6 (images of the powdered Fe(II)-poly sample are provided in ESI,† Fig. S9).

SEM micrographs of the Fe(II)-poly film show the porous nature of the polymer and this was later confirmed by BET surface area analysis using N_2 gas at 77 K (Fig. 6(c)). The polymer shows a reversible isotherm of type-IV, with a small hysteresis and shows a Langmuir surface area of 39 m^2 g^{-1}. The pore size distribution plot is given in the inset of Fig. 6(c), which further confirms the mesoporous nature of the polymer with the pore size between 4 and 42 nm. This pore range closely resembles the pore size obtained by FESEM analysis. Further, the EDAX analysis of the Fe(II)-poly provides the percentage distribution of its components and it has been found that Fe(II) ions are present with 1% abundance with a regular distribution throughout the organic framework (*vide* ESI,† Table S1 and Fig. S10). However, an unexpected percentage distribution of oxygen is shown by EDAX analysis, which is due to the fact that the elemental analysis is performed on the glass substrate which also adds its own energy dispersive spectra along with the appearance of other components of the glass substrate (Table S1, ESI†). The presence of pores throughout the polymer film may allow better transportation of charge/ions through it and thus may enhance the mobility of small molecules/ions through the polymer thin film.

For AFM analysis an even dilute solution (10^{-6} M) of Fe(II)-poly was used to grow a very thin film on a freshly cleaved HOPG substrate. The dilute solution (DMSO:methanol) was injected forcefully from one end of the HOPG surface, so that the polymer chains will detangle and align along the line of force on the HOPG surface, and then kept for drying in a vacuum oven for 12 h. The image of a single polymer strand obtained by AFM, which is shown in Fig. 6(d), shows a Fe(II)-poly thickness

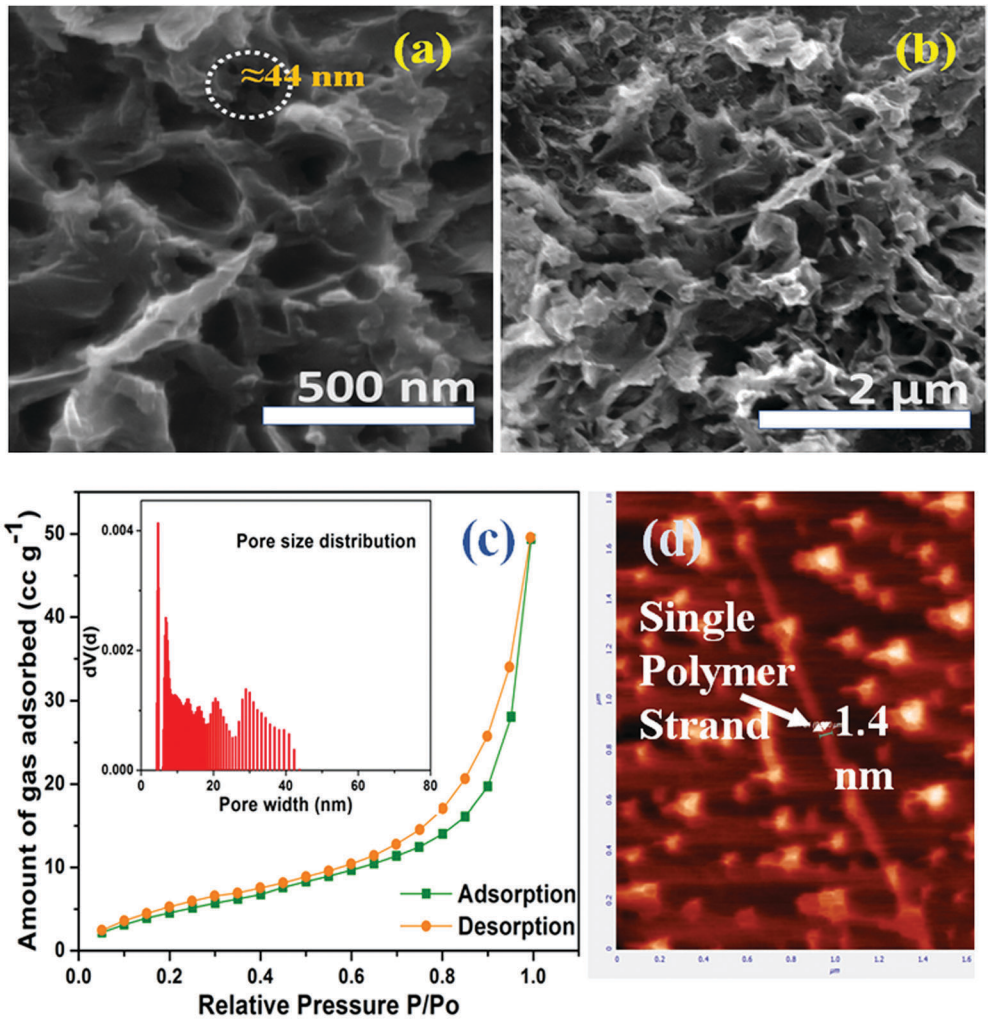

Fig. 6 (a and b) FESEM images of 10^{-5} M solution of Fe(II)-poly on a glass substrate (small pores have been highlighted by a circle with approx. size 44 nm in (a)), (c) N_2 adsorption isotherm of the Fe(II)-poly at 77 K with the pore size distribution in the inset and (d) the single strand of the Fe(II)-poly obtained from AFM on the HOPG substrate.

of 1.4 nm, which closely resembles the calculation of the model structure obtained by MOPAC calculations after energy minimization (*vide* ESI,† Fig. S11).

Electrochemical properties

The redox properties of the free ligand and Fe(II)-poly were studied by CV with glassy carbon as the working electrode, a Pt wire as the counter electrode and Ag/AgCl as the reference electrode in acetonitrile solution containing 0.1 M TBAP at a scanning rate of 100 mV s^{-1}. The voltammograms of Fe(II)-poly are shown in Fig. 7 and that of the ligand are shown in the ESI,† Fig. S12.

The CV results of the ligand showed two reversible cathodic responses in the range of 0 V to −2.0 V (*vide* ESI,† Fig. S12). The reduction at −0.77 V is attributed to the reduction of the first imine group, whereas the second imine group showed reduction at a higher potential (−1.85 V) as the neutral ligand becomes negatively charged after the first reduction and repels incoming electrons for further reduction. This also confirms the very strong bonding in the ligand and because of that strong conjugated bonding, after reduction of the first imine group, the message is passed to the second imine chromophore very fast and it will get reduced at almost double potential than that of the first imine group reduction.

The metallopolymer showed two anodic responses and one cathodic response in the range of −2.0 V to +1.5 V. Anodic responses are due to stepwise oxidation of the Fe(II)–Fe(III) couple and Fe(III)–Fe(IV) couple and the cathodic response is originated from reduction of the organic ligand. As the imine nitrogen is coordinated to the Fe(II)-metal ion in the polymer, a right shift in the cathodic response is observed as the metal ion pulls the electron cloud from the ligand and makes it a more easily reducible substrate than the free ligand.

I–V characterization

The *I–V* curve for the device (*vide* Scheme 3) spun at 1000 rpm is shown in Fig. 8 and it has shown bistability in the conductance. When the voltage was scanned in the positive direction, it first

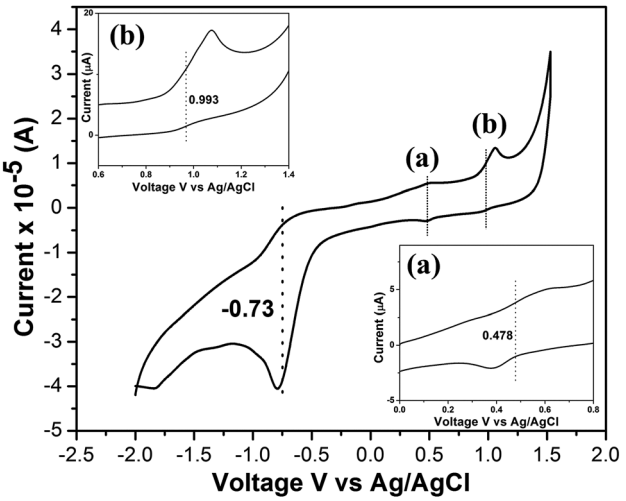

Fig. 7 Cyclic voltammogram of Fe(II)-poly. (inset) Response of the (a) Fe^{2+}/Fe^{3+} redox couple and (b) Fe^{3+}/Fe^{4+} redox couple in acetonitrile solution containing 0.1 M TBAP at 100 mV s^{-1} with glassy carbon as the working electrode and Ag/AgCl as the reference electrode.

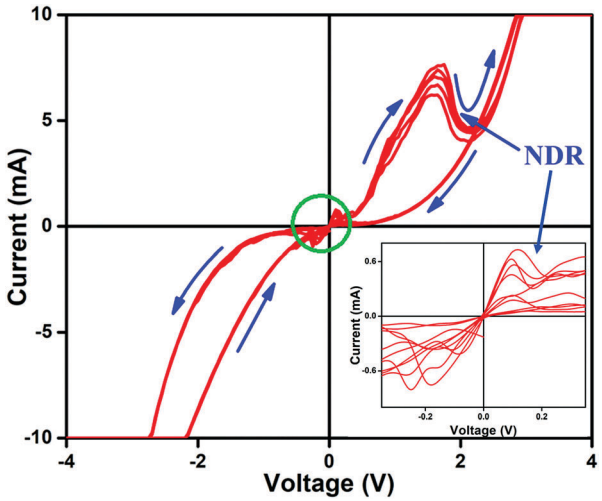

Fig. 8 Current–voltage (*I–V*) graph of Fe(II)-poly scanned between −4.0 V and +4.0 V with the blue arrows showing the direction of the voltage scan. The *I–V* curve for the device is recorded 5 times. The inset shows the zoomed-in area present inside the green circle.

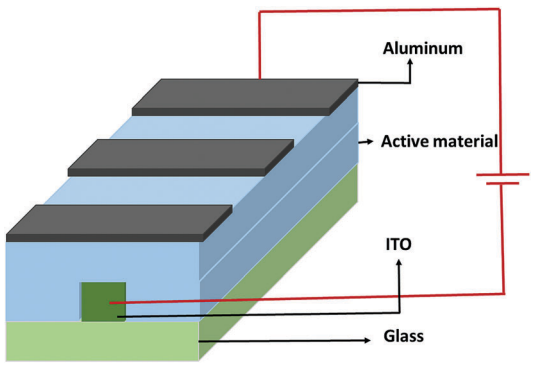

Scheme 3 Device fabrication of Fe(II)-poly as active material.

traces the high current path as shown by the guided arrow (blue) and reaches a local maximum at 0.1 V. This region is zoomed in (green circle) and shown in the inset of Fig. 8. With a further increase in the voltage the current comes down and gives us a short lived local minimum. As the voltage increases further the current also increases till 1.65 V and beyond that the current again decreases till it reaches a valley at 2.1 V, which again is a local minimum. After this point the current again starts increasing till it reaches compliance at 2.95 V and stays there till the scan voltage reaches the maximum at 4 V. When the curve was traced back from the positive voltage toward the negative direction it maintains the compliance current till 2.8 V but after that it follows a high resistive path and continues to follow the negative voltage scan except at −0.2 V where the current goes to a local maximum. After this point the current goes to the low conducting state and remains in the low conducting state till it reaches compliance at −2.75 V and stays in that state till it reaches the maximum voltage in the negative direction at −4 V. When the *I–V* curve was traced back from the negative to the positive bias the current corresponding to the compliance remains there till it reaches −2.2 V. After −2.2 V the *I–V* curve follows the high conducting path till it completes the cycle at 0 V. We have collected hundreds of *I–V* curves and found them to follow the same path reproducibly except in the first few cycles where the second local maximum is shifting towards the high voltage region to a maximum of 1.7 V. So, in this whole process of recording the *I–V* curve, the device shows two negative differential resistance (NDR) peaks on the positive side and one on the negative side of the voltage scan. The maximum On–Off ratio for the device is 11 which is not a significant figure to explain the bistability behaviour of the device, but what is interesting is the NDR feature in the device, which in turn will also reveal the non-volatile memory effect in the device that can be written, erased and read repeatedly.[32] To date only a few reports of hybrid materials exhibiting the NDR effect have been reported[55] and our initial attempts at the study of our synthesized economical novel hybrid polymer have shown this remarkable behaviour.

We can explain the NDR behaviour of the device by understanding the structure of the molecule. The molecule is doubly reduced by accepting two electrons and when the electron is captured in one of the sites (nitrogen) of the molecule, that point acts as a quantum well for the electron and unless a suitable resonant energy is provided to the molecule, the transport through the molecule will be restricted and hence there is a decrease in the current through the device (after 0.1 V). But at some higher voltage the electron will be released and the current again starts to increase till two electrons are captured at two different sites (nitrogen) of the molecule. This will again reduce the current through the device and after a particular voltage, it will start increasing again. This process also accompanies a metal filament formation by reaching the compliance current. This is a process which follows the high conducting pathway, but as we retrace back toward the negative bias, it goes through the low conducting path, because the metal filament starts breaking

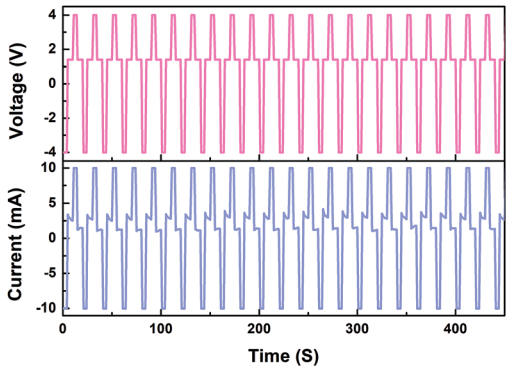

Fig. 9 The RAM application of the device was studied by using a write, erase, and read voltage pulse of 4 V, −4 V, and 1.4 V respectively. The pulse width was of 1 second and was applied for 4, 4, and 6 s respectively.

out and the current starts decreasing. The current will increase with the increase in negative bias but will follow a low conducting pathway. The current will reach compliance and when we retrace back from negative to positive side it follows a high conducting path.

We studied the random access memory (RAM) feature for the device where we used the write, read, erase, and read sequence as 4 V, 1.4 V, −4 V, and 1.4 V respectively (*vide* Fig. 9). We have chosen 1.4 V as the read voltage because the On–Off ratio is maximum at that voltage. We found that the device is reading the memory reproducibly at each read sequence after the write and erase voltage. The write and erase sequence would run for 4 s at a gap of 0.5 s and the read sequence will run for 6 s at a gap of 0.5 s. We run 1000 such cycles and found that the reading is consistent and the states are reproducible. Here we have shown only a part of the whole sequence.

The read only memory (ROM) application was also tested for the device by observing its retention characteristics and here also the device showed consistent performance (*vide* Fig. 10). The write and erase sequences were run for 20 s with a write and erase voltage pulse of 4 and −4 V with a pulse width of 0.5 s and at a gap of 0.5 s, and then the states were probed by using a read voltage pulse of 1.4 V. It was found that the read voltage pulse after the write and erase pulse retains the states efficiently even after 2000 s. This long retention time of the device is important for practical memory applications.

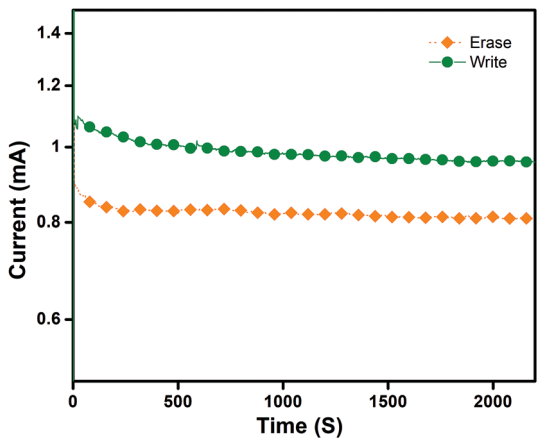

Fig. 10 The ROM application of the device was studied by applying a write voltage of 4 V of width one second for 20 s and probed with a read voltage of 1.4 V for more than 2000 s. Similarly an erase voltage of −4 V of width 1 s for 20 s followed by a read voltage of 1.4 V for more than 2000 s to probe the erase state of the device.

Conclusions

We have successfully synthesized and characterized the Schiff's base ligand **L1**. Fe(II)-poly has been fully characterized by NMR, FTIR, and other techniques. The coordination capability of the ligand and model ligand shows some remarkable differences with the same metal ions although the model ligand is just one-half of the original ligand but both have the same coordination sites. Both ligand and polymer have shown reversible redox activity. The memory behaviour of Fe(II)-poly has shown bistability with a unique Negative Differential Resistance (NDR) effect, which is crucial for state-of-the-art electronic devices. The observed reproducible nature of the device with consistent performance for more than 1000 cycles shows the potential application of the device in RAM devices. The prolonged retention time of more than 2000 s shows ROM performance of the device. Although the retention time and the switching cycle are still far from satisfactory when compared to the current Si technology, the research on organic memory is still in its infancy, and its device performance is expected to increase by tuning of the ligand structure and fabrication process. Therefore this novel polymer has great potential for future memory devices.

Funding source

Financial support received from the Science and Engineering Research Board, DST New Delhi (under the grant EMR/2016/001994), is acknowledged. DO is grateful to the Council of Scientific and Industrial Research, New Delhi, for her fellowship. US is thankful to MHRD for financial support.

Conflicts of interest

There are no conflicts to declare.

Acknowledgements

Thanks are due to Dr Suman Mukhopadhyay of IIT Indore, and Dr Kaushik Ghosh and Dr Paritosh Mohanty of IIT Roorkee for their kind help. We thank Mr Bidyut Kumar Kundu of IIT Indore for performing the cyclic voltammetry experiment. DO is also highly thankful to Mrs Monika Chaudhary of IIT Roorkee.

References

1 S. K. Deb, *Appl. Opt.*, 1969, **8**, 192–195.
2 F. S. Han, M. Higuchi, Y. Akasaka, Y. Otsuka and D. G. Kurth, *Thin Solid Films*, 2008, **516**, 2469–2473.

3 M. Higuchi, *Polym. J.*, 2009, **41**, 511–520.
4 A. Bandyopadhyay and M. Higuchi, *Eur. Polym. J.*, 2013, **49**, 1688–1697.
5 L. O. Chua and S. M. Kang, *Proc. IEEE*, 1976, **64**, 209–223.
6 A. Bandyopadhyay, S. Sahu and M. Higuchi, *J. Am. Chem. Soc.*, 2011, **133**, 1168–1171.
7 S. Goswami, A. J. Matula, S. P. Rath, S. Hedström, S. Saha, M. Annamalai, D. Sengupta, A. Patra, S. Ghosh, H. Jani, S. Sarkar, M. R. Motapothula, C. A. Nijhuis, J. Martin, S. Goswami, V. S. Batista and T. Venkatesan, *Nat. Mater.*, 2017, **16**, 1216–1224.
8 A. Serres, M. Baudyš and S. W. Kim, *Pharm. Res.*, 1996, **13**, 196–201.
9 P. Gupta, K. Vermani and S. Garg, *Drug Discovery Today*, 2002, **7**, 569–579.
10 H. Ahn, J. Hong, S. Y. Kim, I. Choi and M. J. Park, *ACS Appl. Mater. Interfaces*, 2015, **7**, 704–712.
11 E. Fukada, *IEEE Trans. Ultrason. Eng.*, 2000, **47**, 1277–1290.
12 K. S. Ramadan, D. Sameoto and S. Evoy, *Smart Mater. Struct.*, 2014, **23**, 033001.
13 M. Irie, *Chem. Rev.*, 2000, **100**, 1685–1716.
14 R. Pardo, M. Zayat and D. Levy, *Chem. Soc. Rev.*, 2011, **40**, 672.
15 P. Kiria, G. Hyett and R. Binionsa, *Adv. Mater. Lett.*, 2010, **1**, 86–105.
16 Y. Wang, E. L. Runnerstrom and D. J. Milliron, *Annu. Rev. Chem. Biomol. Eng.*, 2016, **7**, 283–304.
17 M. Burnworth, L. Tang, J. R. Kumpfer, A. J. Duncan, F. L. Beyer, G. L. Fiore, S. J. Rowan and C. Weder, *Nature*, 2011, **472**, 334–337.
18 F. Niroui, A. I. Wang, E. M. Sletten, Y. Song, J. Kong, E. Yablonovitch, T. M. Swager, J. H. Lang and V. Bulović, *ACS Nano*, 2015, **9**, 7886–7894.
19 S. Förster and M. Konrad, *J. Mater. Chem.*, 2003, **13**, 2671–2688.
20 B. M. Novak, *Adv. Mater.*, 1993, **5**, 422–433.
21 L. D. Carlos, R. A. S. Ferreira, V. De Zea Bermudez, B. Julián-López and P. Escribano, *Chem. Soc. Rev.*, 2011, **40**, 536–549.
22 L. Wang, M. H. Yoon, A. Facchetti and T. J. Marks, *Adv. Mater.*, 2007, **19**, 3252–3256.
23 C. R. Kagan, D. B. Mitzi and C. D. Dimitrakopoulos, *Science*, 1999, **286**, 945–947.
24 J. Even, L. Pedesseau, J. M. Jancu and C. Katan, *J. Phys. Chem. Lett.*, 2013, **4**, 2999–3005.
25 P. Gómez-Romero, M. Chojak, K. Cuentas-Gallegos, J. A. Asensio, P. J. Kulesza, N. Casañ-Pastor and M. Lira-Cantú, *Electrochem. Commun.*, 2003, **5**, 149–153.
26 H. Kim, S. H. Jo, J. H. Jee, W. J. Han, Y. Kim, H. H. Park, H. J. Jin, B. Yoo and J. K. Lee, *New J. Chem.*, 2015, **39**, 836–842.
27 B. Hu, C. Wang, J. Wang, J. Gao, K. Wang, J. Wu, G. Zhang, W. Cheng, B. Venkateswarlu, M. Wang, P. S. Lee and Q. Zhang, *Chem. Sci.*, 2014, **5**, 3404–3408.
28 C.-L. Liu and W.-C. Chen, *Polym. Chem.*, 2011, **2**, 2169.
29 B.-B. Cui, Z. Mao, Y. Chen, Y.-W. Zhong, G. Yu, C. Zhan and J. Yao, *Chem. Sci.*, 2015, **6**, 1308–1315.
30 C. Wang, P. Gu, B. Hu and Q. Zhang, *J. Mater. Chem. C*, 2015, **3**, 10055–10065.
31 P. Routh, R. K. Layek and A. K. Nandi, *Carbon*, 2012, **50**, 3422–3434.
32 J. Lin, M. Zheng, J. Chen, X. Gao and D. Ma, *Inorg. Chem.*, 2007, **46**, 341–344.
33 U. Tritschler, F. Beck, H. Schlaad and H. Colfen, *J. Mater. Chem. C*, 2015, **3**, 950–954.
34 P. Ferreira, R. Z. Hou, A. Wu, M. G. Willinger, P. M. Vilarinho, J. Mosa, C. Laberty-Robert, C. Boissière, D. Grosso and C. Sanchez, *Langmuir*, 2012, **28**, 2944–2949.
35 B. J. Scott, G. Wirnsberger and G. D. Stucky, *Chem. Mater.*, 2001, **13**, 3140–3150.
36 Y. S. Lin, S. H. Wu, Y. Hung, Y. H. Chou, C. Chang, M. L. Lin, C. P. Tsai and C. Y. Mou, *Chem. Mater.*, 2006, **18**, 5170–5172.
37 K. Yan, B. Chen, H. Hu, S. Chen, B. Dong, X. Gao, X. Xiao, J. Zhou and D. Zou, *Adv. Electron. Mater.*, 2016, **2**, 1–7.
38 V. Lyaskovskyy and B. De Bruin, *ACS Catal.*, 2012, **2**, 270–279.
39 C. Kaes, A. Katz and M. W. Hosseini, *Chem. Rev.*, 2000, **100**, 3553–3590.
40 S. Kumar, D. N. Dhar and P. N. Saxena, *J. Sci. Ind. Res.*, 2009, **68**, 181–187.
41 H. Niu, H. Kang, J. Cai, C. Wang, X. Bai and W. Wang, *Polym. Chem.*, 2011, **2**, 2804.
42 B. Pradhan and S. Das, *Chem. Mater.*, 2008, **20**, 1209–1211.
43 T. L. Choi, K. H. Lee, W. J. Joo, S. Lee, T. W. Lee and Y. C. Mi, *J. Am. Chem. Soc.*, 2007, **129**, 9842–9843.
44 Y. Z. Tang, M. Zhou, J. Huang, Y. H. Tan, J. S. Wu and H. R. Wen, *Inorg. Chem.*, 2013, **52**, 1679–1681.
45 S. Guieu, *Synth. Commun.*, 2012, **42**, 3177–3186.
46 B. Comesaña-Gándara, M. Calle, H. J. Jo, A. Hernández, J. G. de la Campa, J. de Abajo, A. E. Lozano and Y. M. Lee, *J. Membr. Sci.*, 2014, **450**, 369–379.
47 G. Bhagavannarayana, R. V. Ananthamurthy, G. C. Budakoti, B. Kumar and K. S. Bartwal, *J. Appl. Crystallogr.*, 2005, **38**, 768–771.
48 L. Legrand, M. Abdelmoula, a. Géhin, a. Chaussé and J.-M. R. Génin, *Electrochim. Acta*, 2001, **46**, 1815–1822.
49 J. Matijevi and M. Vinkovi, *Croat. Chem. Acta*, 2006, **79**, 489–495.
50 P. B. Tsitovich, F. Gendron, A. Y. Nazarenko, B. N. Livesay, A. P. Lopez, M. P. Shores, J. Autschbach and J. R. Morrow, *Inorg. Chem.*, 2018, **57**, 8364–8374.
51 D. Sharma, S. K. Sahoo, R. K. Bera and R. Kamal, *J. Fluoresc.*, 2013, **23**, 387–392.
52 X. Wang, X. Chen, A. Thomas, X. Fu and M. Antonietti, *Adv. Mater.*, 2009, **21**, 1609–1612.
53 R. Dholam, N. Patel, M. Adami and A. Miotello, *Int. J. Hydrogen Energy*, 2009, **34**, 5337–5346.
54 T. Sato, R. K. Pandey and M. Higuchi, *Dalton Trans.*, 2013, **42**, 16036–16042.
55 C. Wu, F. Li, Y. Zhang, T. Guo and T. Chen, *Appl. Phys. Lett.*, 2011, **99**, 2009–2012.

